ACCSCIENCE PUBLISHING

International Journal of Bioprinting

RESEARCH ARTICLE

Therapeutic effects of 3D-bioprinted mesenchymal stem cell-based artificial lymph nodes on lymphedema

Hyo Jin Kang[1†], Ju-Hee Lee[2†], Yong Xun Jin[3], Yujin Myung[3], and Jae Hoon Jeong[3*]

[1]Department of Biomedical Laboratory Science, College of Health Sciences, Honam University, Gwangju, Republic of Korea

[2]Department of Korean Medicine, College of Korean Medicine, Dongguk University, Goyang, Gyeonggi-do, Republic of Korea

[3]Department of Plastic and Reconstructive Surgery, Seoul National University Bundang Hospital, Seoul National University College of Medicine, Seongnam, Gyeonggi-do, Republic of Korea

Abstract

Lymphedema is a condition resulting from impaired lymphatic function, with limited effective treatment options available. This study investigates the potential of 3D-bioprinted scaffolds, utilizing biomaterials and human adipose-derived stem cells (hADSCs), as a novel approach to promote lymphangiogenesis and improve treatment outcomes in lymphedema. Scaffolds were characterized for cell viability, mechanical properties through compressive strength testing, and structural integrity after printing. *In vivo* therapeutic effects were assessed in Sprague–Dawley rats through fluorescence imaging, histopathological analysis, and immunofluorescence staining. Additionally, protein and gene expression of lymphangiogenic markers (LYVE-1, VEGF-C, VEGF-A) were analyzed using Western blotting and quantitative polymerase chain reaction. The scaffolds demonstrated high cell viability, structural integrity, and mechanical stability, with enhanced cell distribution and extracellular matrix deposition over time. Scaffolds containing hADSCs showed the most lymph node-like characteristics, with a well-defined capsule and increased lymphocytic infiltration. Immunofluorescence analysis revealed enhanced expression of LYVE-1, Prox1, and CD31, indicating significant lymphatic and vascular remodeling. Additionally, upregulation of LYVE-1, VEGF-C, and VEGF-A protein and mRNA levels highlighted the scaffolds' potential in promoting lymphangiogenesis and angiogenesis. These findings highlight the significant potential of hADSCs-loaded scaffolds in enhancing tissue regeneration, particularly in restoring lymphatic function in lymphedema.

Keywords: Bioprinting; Lymphedema; Lymph nodes; Lymphangiogenesis; Mesenchymal stem cells; Tissue engineering

†These authors contributed equally to this work.

***Corresponding authors:**
Jae Hoon Jeong
(psdrj2h@gmail.com)

Citation: Kang, HJ, Lee JH, Jin YX, Myung, Y, Jeong JH. Therapeutic effects of 3D-bioprinted mesenchymal stem cell-based artificial lymph nodes on lymphedema. *Int J Bioprint.* 2025;11(3):457-474 doi: 10.36922/IJB025140124

Received: April 5, 2025
1st revised: May 1, 2025
2nd revised: May 14, 2025
Accepted: May 15, 2025
Published online: May 15, 2025

1. Introduction

Lymphedema is a persistent condition marked by the buildup of lymphatic fluid, resulting in swelling and tissue fibrosis.[1] This typically occurs due to impairment of

the lymphatic system caused by surgical procedures, radiation treatment, or infections.[2] This condition is especially common following cancer treatments, including lymph node excision, and it has a considerable impact on patients' quality of life.[3] Existing therapeutic modalities, including manual lymphatic drainage, compression garments, and surgical procedures, demonstrate restricted long-term effectiveness and frequently do not achieve complete restoration of lymphatic function.[4,5] Thus, there is an urgent need for innovative approaches that can effectively regenerate the lymphatic network and promote lymphangiogenesis.

Recent research has emphasized the promise of human adipose-derived stem cells (hADSCs) in tissue regeneration, attributable to their capacity to differentiate into multiple cell types and release growth factors that assist tissue repair.[6–8] Decellularized lymph node scaffolds have proven to be effective instruments in lymphatic tissue engineering, preserving the fundamental structure of lymph nodes while eliminating cellular elements that could trigger immune reactions.[9,10] A recent study emphasized that the integration of hADSCs with decellularized lymph node scaffolds shows considerable promise in enhancing lymphangiogenesis and reducing lymphedema in animal models.[11] Nonetheless, obstacles persist in attaining ideal cell distribution and maintaining scaffold integrity to ensure long-term therapeutic effectiveness.

In response to these challenges, 3D bioprinting technology offers a novel solution to precisely control the deposition of cells and biomaterials, creating highly structured and customized scaffolds for tissue regeneration.[12,13] 3D bioprinting allows for the creation of complex tissue architectures with cellular components that can more closely mimic the native microenvironment of the lymphatic system.[14] By integrating hADSCs with biocompatible scaffolds in a controlled, reproducible manner, it is possible to optimize cell distribution, support lymphangiogenesis, and enhance therapeutic outcomes for lymphedema treatment.[15]

Several bioprinting techniques have been developed to fabricate cell-laden scaffolds, including extrusion-based printing, inkjet printing, and vat photopolymerization.[15] Inkjet bioprinting uses thermal or piezoelectric pulses to eject droplets of bioink, allowing rapid and high-resolution printing. However, it is restricted to low-viscosity bioinks and is prone to nozzle clogging, making it less suitable for viscous or cell-rich formulations.[16] Vat photopolymerization enables fine structural fabrication but is limited to photocurable materials, which may pose cytotoxic risks and are often incompatible with physiological conditions.[17] Moreover, the influence of each bioprinting modality on cell viability has been increasingly studied. Inkjet-based bioprinting may cause significant shear and thermal stress on cells due to droplet generation dynamics, affecting their viability.[18] Vat photopolymerization involves photoinitiators and ultraviolet (UV) exposure, which may lead to cytotoxicity depending on exposure dose and initiator concentration.[19] Extrusion-based printing subjects cells to shear stress within the nozzle and during material deposition; however, it allows the use of shear-thinning hydrogels and can maintain acceptable viability when optimized.[20] These considerations informed our decision to adopt extrusion-based bioprinting in this study.

In addition to its compatibility with living cells, extrusion-based bioprinting, by contrast, supports a broader range of biomaterials, including shear-thinning and high-viscosity bioinks, and operates under mild, cell-friendly conditions. Its adaptability makes it ideal for printing hydrogels laden with cells or extracellular matrix (ECM) components.[21,22] Given these advantages, we selected extrusion-based bioprinting for this study to facilitate the controlled deposition of alginate–atelocollagen composite bioinks and create stable, functional scaffolds for lymphatic tissue regeneration.

The aim of this study is to evaluate the potential of 3D-bioprinted scaffolds, composed of a suitable biomaterial and hADSCs, in the treatment of lymphedema. By using a 3D bioprinting approach, we intend to create a more efficient and stable recellularized lymph node model to investigate the therapeutic effects on lymphangiogenesis. We will conduct a thorough evaluation of the effectiveness of these 3D-printed constructs in animal models of lymphedema, benchmarked against conventional stem cell therapies, and decellularized lymph node scaffolds.

2. Materials and methods

2.1. 3D bioprinting

To prepare the bioink, sodium alginate (viscosity ≥ 2000 cP, 25°C) (A2033, Sigma Aldrich, USA) was dissolved in distilled water at 37°C for 24 h to achieve a final concentration of 3% w/v. For atelocollagen preparation, the collagen sponge was acidified in 0.001N HCl at 4°C for 24 h to reach a concentration of 6% w/v. The solution was then neutralized by mixing with 132 mM Na_2HPO_4 at a 1:1 ratio and stored at 4°C. The bioink was formulated by blending atelocollagen and sodium alginate at a 4:1 ratio (for Group 3; see Section 2.3 for group definition). To prepare a cell-laden bioink, human adipose-derived mesenchymal stem cells (human ADMSCs; #7510, ScienCell, USA) at a density of 1×10^6 cells/mL were incorporated into the bioink mixture (for Group 4; see Section 2.3 for group definition). The rheological properties of the bioink were

assessed using a rheometer (MCR 102e, Anton Paar, Germany) equipped with a 1.0 mm gap and 25 mm parallel plates under a controlled temperature of 4°C. Scaffolds were fabricated using an extrusion-based 3D bioprinter (Baobab Root-1, Baobab Healthcare Inc., Republic of Korea). Both cell-free and cell-laden bioinks were printed into cylindrical scaffolds (diameter: 5 mm, height: 5 mm) using a 25G tapered nozzle. The printing parameters were set at a pneumatic pressure of 20 kPa and a printing speed of 300 mm/min. Post-printing, the structural integrity of the scaffolds was maintained by applying 200 mM $CaCl_2$ for 10 s to induce ionic crosslinking of alginate. The constructs were then incubated at 37°C for 30 min to facilitate the physical crosslinking of atelocollagen (Figure 1A).

2.2. Cell viability and mechanical characterization

The viability of hADSCs within the scaffolds was assessed using a LIVE/DEAD™ Viability/Cytotoxicity Kit (L3324, Invitrogen™, USA) after 5 days of culture. The live and dead cells were visualized to evaluate cell survival rates. For comparison, hADSCs were also cultured under conventional 2D monolayer conditions using tissue culture-treated plates, maintained in the same growth medium, and incubated at 37°C with 5% CO_2 without being subjected to the bioprinting process. To examine the mechanical properties of the scaffolds, compressive strength was measured using a universal testing machine (QM100s, QMESYS, Republic of Korea) at 37°C with a crosshead speed of 1 mm/min. The impact of increased cell density following culture was also assessed by evaluating physical changes in the scaffold structure.

2.3. Animals

Seven-week-old male Sprague–Dawley (SD) rats, with weights ranging from 220 to 250 g, were obtained from ORIENT BIO (Seongnam, Republic of Korea) and were housed in compliance with the standards established by the Association for Assessment and Accreditation of Laboratory Animal Care International (AAALAC). All animal-related procedures conformed to the guidelines set forth in the International Guide for the Care and Use of Laboratory Animals. Besides, the study received approval

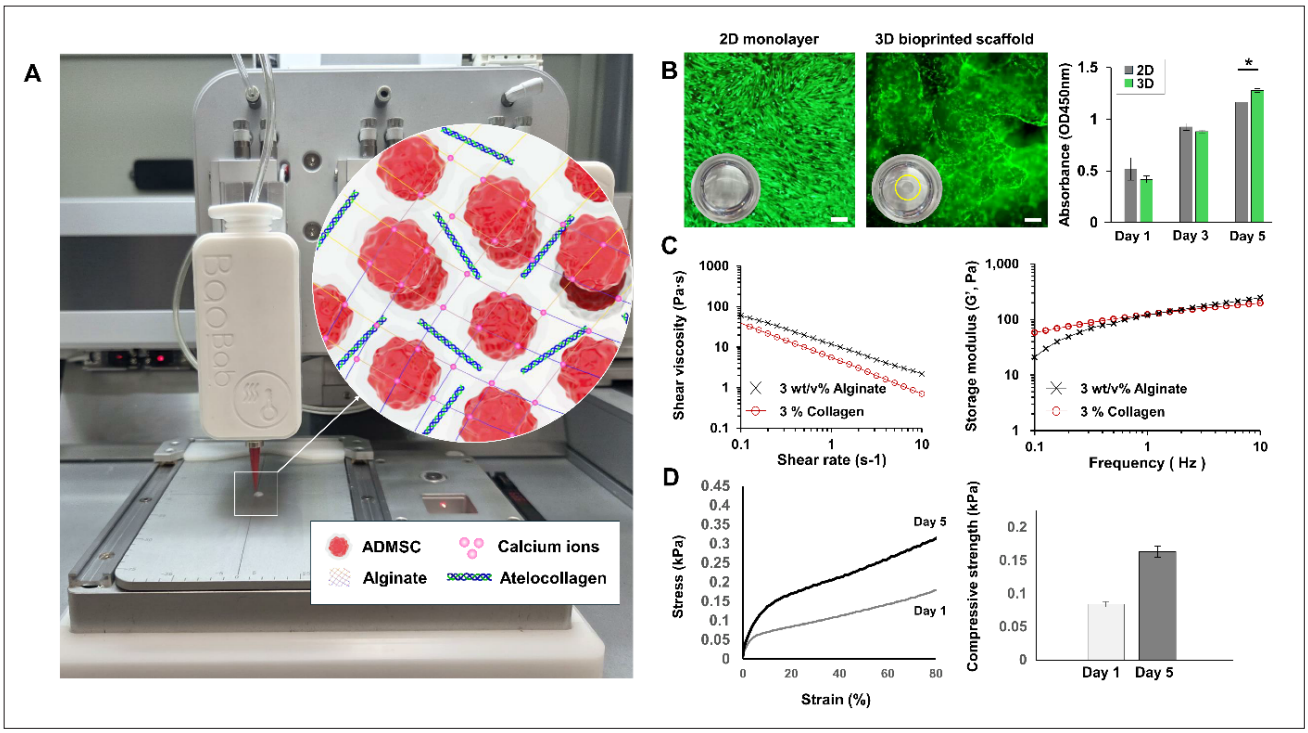

Figure 1. Evaluation of 3D-bioprinted constructs: structural, cellular, and mechanical properties. (A) Schematic representation of the 3D bioprinting process, including bioink composition (sodium alginate and atelocollagen), hADSCs, and the extrusion-based printing methodology. (B) Live/Dead staining of 3D-printed scaffolds after 5 days of culture, demonstrating high cell viability and uniform distribution of hADSCs within the scaffold matrix, compared to 2D culture. (C) The compressive strength of the scaffolds was measured over 5 days, showing a progressive increase in stiffness indicative of ECM deposition and structural reinforcement. (D) Quantitative analysis of the compressive modulus, confirming mechanical maturation of the scaffolds over time. The scaffolds maintained well-defined cylindrical shapes (5 mm diameter × 5 mm height) post-crosslinking, and rheological analysis demonstrated shear-thinning behavior, enabling smooth extrusion and shape retention during printing. Abbreviations: ADMSC, adipose-derived mesenchymal stem cell; hADSCs, human adipose-derived stem cells.

from the Institutional Animal Care and Use Committee (IACUC) at Seoul National University Bundang Hospital (IACUC No. BA-2308-374-002-04). The study was carried out in accordance with the ARRIVE guidelines. A total of 40 SD rats were randomly divided into following four experimental groups: the lymphedema control group (Group 1, G1); the hADSC group (Group 2, G2); the blank scaffold (3D bioprinting scaffold) (Group 3, G3); and the hADSCs scaffold (3D bioprinting scaffold containing hADSCs) (Group 4, G4). Rats were anesthetized through inhalation of 2% isoflurane. To assist in the identification of lymph nodes, a subcutaneous injection of 10% Evans blue dye (Glentham Life Sciences, Corsham, London, UK) was administered in both hind feet of the rats. After performing bilateral femoral incisions, the inguinal lymph nodes were identified and removed. Subject to the experimental group, rats were administered injections of hADSCs, the blank scaffold, or the hADSCs scaffold. Following the procedures, the incisions were closed with sutures. To assess the severity of lymphedema and the therapeutic effects of treatment, we measured both mid-thigh circumference and paw thickness in the hindlimbs of all rats. A total of 40 rats (n = 10 per group) were evaluated. Measurements were taken on both the affected (left) and unaffected (right) limbs using a flexible measuring tape (for thigh circumference) and a digital caliper (for paw thickness). The mid-thigh circumference ratio and paw thickness ratio were calculated by dividing the measurement of the affected limb by that of the contralateral, unaffected limb. Measurements were performed at the same anatomical landmarks for all animals to ensure consistency: mid-thigh circumference was recorded at the midpoint between the inguinal crease and the knee joint, while paw thickness was measured at the thickest point of the dorsal hind paw.

2.4. Indocyanine green video imaging

The indocyanine green (ICG; 2.5 mg/mL in normal saline) solution was prepared by dissolving ICG (*Dong-in Dang Pharmaceutical* Co., Siheong, *Korea*) prior to injection.[23,24] **ICG** was administered to the rats through a subcutaneous injection of 0.1 mL of ICG solution into the foot using 30G needle. Immediately following the injection of ICG, infrared fluorescence imaging was conducted using the Fluotics System (Fluobeam®, Fluoptics, France). Images were taken at baseline and at key intervals post-injection to track ICG distribution over time (Video S1, Supporting Information). ICG lymphography was performed in a total of 12 rats, with 3 animals per group (n = 3 per group). Dermal backflow patterns were assessed using the arm dermal backflow (ADB) scale, which grades the severity of dermal lymphatic reflux as follows: stage 0—linear pattern (normal), stage 1—splash or stardust pattern (mild backflow), stage 2—diffuse pattern (moderate to severe backflow), and stage 3—no visible lymphatic vessels (complete dermal reflux). Lymphatic vessel visualization was qualitatively evaluated by two independent investigators blinded to group allocation. Visibility was categorized as either "clear" (distinct vessel outline) or "blurred" (poorly defined or absent). Tracer clearance was determined based on fluorescence persistence over time. An overall lymphatic recovery grade (poor/good) was assigned based on a composite evaluation of the three parameters.

2.5. Histopathological assessment

A total of 40 rats (n = 10 per group) were subjected to histopathological assessment. Tissues were fixed in 10% formalin and embedded in paraffin. The samples were routinely processed and sectioned into 4–5 μm thick slices. The sections were then deparaffinized in xylene at room temperature and stained with hematoxylin and eosin (Cancer Diagnostics Inc., Durham, NC, USA) according to the manufacturer's instructions. For Masson's trichrome staining (BBC Biochemical, Mount Vernon, WA, USA), deparaffinized sections were first fixed in Bouin's solution for 1 h at 56°C. The sections were then stained with ClearView Iron Hematoxylin working solution for 10 min, followed by sequential staining with Biebrich scarlet-acid fuchsin solution for 2 min, phosphomolybdic-phosphotungstic acid solution for 10 min, aniline blue solution for 3 min, and 1% acetic acid solution for 2 min. As a result, ECM, collagen, and other connective tissue components appeared blue, while smooth muscle fibers were stained red. Finally, the stained tissue sections were imaged at 400× magnification using a slide scanner (3DHISTECH Ltd, Budapest, Hungary).

2.6. Immunofluorescence analysis

Tissue sections were deparaffinized in xylene and rehydrated through a graded ethanol series. Heat-induced epitope retrieval was performed in citrate buffer (pH 6.0; Scytek Laboratories, Inc., West Logan, UT, USA) at 56°C for 40 min. The sections were then incubated with 3% bovine serum albumin (BSA) blocking reagent for 10 min at room temperature. Next, the sections were incubated with primary antibodies, including anti-LYVE-1 (Abcam Inc., CA, USA), anti-Prox1 (Thermofisher Scientific, MA, USA), and anti-CD-31 (Abcam Inc., CA, USA), at a 1:100 dilution for 90 min at room temperature. This was followed by incubation with Alexa Fluor 488- and Alexa Fluor 594-conjugated secondary antibodies (1:500; BioLegend, San Diego, CA, USA). The sections were then mounted using a DAPI-containing mounting medium (Vector Laboratories Inc., Burlingame, CA, USA) and visualized under an inverted microscope (Zeiss MicroImaging GmbH, Jena, Germany). The immunofluorescence analysis

was performed in a total of 20 rats, with 5 animals per group (n = 5 per group). The quantitative image analysis was conducted using ImageJ software (NIH, USA). The fluorescence intensity of individual markers (LYVE-1, Prox1, CD31) and merged signals (LYVE-1 + Prox1, LYVE-1 + CD31) were measured from five randomly selected high-power fields per specimen.

2.7. Western blotting

Tissues were homogenized in PRO-PREP™ Protein Extraction Solution (iNtRON Biotechnology, Seongnam, Korea) containing phosphatase and protease inhibitors (GenDEPOT Inc., Barker, TX, USA). Protein concentrations were measured using a NanoDrop Lite spectrophotometer (Thermo Fisher Scientific, Waltham, MA, USA) following the manufacturer's protocol. Equal amounts of protein were mixed with 4× Laemmli sample buffer (Bio-Rad Laboratories Inc., Hercules, CA, USA), denatured at 95°C for 10 min, separated on 10% sodium dodecyl sulfate–polyacrylamide gels, and transferred onto Immobilon®-P PVDF membranes (0.45 μm pore size, Merck Millipore, Darmstadt, Germany) using EzFastBlot (ATTO, Tokyo, Japan). Membranes were blocked with 5% skim milk solution for 1 h at room temperature and incubated overnight at 4°C with primary antibodies against LYVE-1 (1:1000; NOVUS, Briarwood, CO, USA), VEGF-C (1:500; Santa Cruz Biotechnology, Santa Cruz, CA, USA), VEGF-A (1:500; Abcam, Cambridge, UK), and β-actin (1:1000; Santa Cruz Biotechnology). After washing with 1× PBST (phosphate-buffered saline containing 0.1% Tween-20), membranes were incubated for 1 h at room temperature with horseradish peroxidase-conjugated secondary antibodies (1:2000; anti-mouse IgG or anti-rabbit IgG; Cell Signaling Technology, Danvers, MA, USA). Protein bands were visualized using the West-Q Pico Dura or Femto Clean ECL Solution (GenDEPOT Inc.) and imaged using the Fusion Solo 2M chemiluminescence imaging system from Vilber Lourmat (Marne-la-Vallée, France). Band intensities were quantified using ImageJ software (version 1.52a, National Institutes of Health, Bethesda, MD, USA), with protein expression levels normalized to β-actin and expressed relative to control values. Western blot analysis was performed in a total of 12 rats, with 3 animals per group (n = 3 per group).

2.8. Quantitative real time-polymerase chain reaction (qRT-PCR)

Total RNA was extracted from tissue samples using TRI reagent® (Molecular Research Center, Inc., Cincinnati, OH, USA) according to the manufacturer's protocol. The extracted RNA was quantified using a NanoDrop Lite spectrophotometer (Thermo Fisher Scientific), and cDNA was synthesized using AccuPower® RT PreMix (BIONEER, Daejeon, Korea). The reverse transcription was conducted at 42°C for 1 h, followed by enzyme inactivation at 95°C for 5 min using a T100 Thermal Cycler (Bio-Rad Laboratories Inc., Hercules, CA, USA). The mRNA levels of LYVE-1, VEGF-C, VEGF-A, and GAPDH (glyceraldehyde-3 phosphate dehydrogenase) were quantified via real-time PCR. The cDNA, along with gene-specific primers and KAPA SYBR® FAST Universal reagent (Roche, Basel, Switzerland), was amplified on a LightCycler® 96 Real-Time PCR System (Roche). Data acquisition and analysis were conducted using the LightCycler® 96 SW 1.1 program (Roche). GAPDH was used as the reference gene to normalize target gene expression levels. Relative mRNA expression was calculated using the comparative Ct ($2^{-\Delta\Delta Ct}$) method. The sequences of the primers used were as follows: LYVE-1 (Forward 5'-CCA GCA GGA ACC AGG TGG AAT C-3', Reverse 5'-AGG TGT CAG ATG AGT TGT GGC AAT-3'); VEGF-C (Forward 5'-TCT TGT CTC TGG CGT GTT CCT T-3', Reverse 5'-CAC AGA CCG CAA CTG CTC CT-3'); VEGF-A (Forward 5'-ATC CTG GAG CGT TCA CTG-3', Reverse 5'-TCA CCG CCT TGG CTT GTC-3'); GAPDH (Forward 5'-TCT CTG CTC CTC CCT GTT C-3', Reverse 5'-ACA CCG ACC TTC ACC ATC T-3'). The qRT-PCR analysis was also conducted in the same 12 rats (n = 3 per group).

2.9. Statistical analysis

All experiments were conducted independently at least three times. Data are expressed as the mean ± standard error of the mean (SEM). Statistical analyses were conducted using one-way analysis of variance (ANOVA), followed by Tukey's or Dunn's post hoc test to assess differences between groups. All analyses were performed using GraphPad Prism software (GraphPad Software Inc., San Diego, CA, USA). A p-value of less than 0.05 was considered statistically significant.

3. Results

3.1. Evaluation of 3D-bioprinted constructs: structural, cellular, and mechanical properties

The selection of bioink composition, cell types, and bioprinting methodology was driven by the need to achieve high cell viability, structural integrity, and biocompatibility for tissue regeneration. Sodium alginate was chosen for its ability to provide rapid ionic crosslinking, ensuring immediate scaffold formation and stability. Atelocollagen was incorporated to enhance cellular adhesion and mimic the ECM, promoting cell proliferation and differentiation. The combination of alginate and atelocollagen created an optimal microenvironment for hADSCs, supporting their viability and functionality. Extrusion-based 3D bioprinting was selected due to its capacity to accommodate bioinks of

varying viscosities while maintaining structural precision. The Baobab Root-1 bioprinter enabled the fabrication of uniform cylindrical scaffolds with a controlled deposition process, ensuring reproducibility. The use of a 25G tapered nozzle allowed fine resolution, while a controlled pneumatic pressure (20 kPa) and printing speed (300 mm/min) facilitated consistent construct formation. The dual crosslinking approach—calcium chloride ($CaCl_2$) for alginate gelation and thermal incubation for atelocollagen stabilization—was crucial for scaffold integrity and prolonged mechanical stability. This combination of ionic and thermal crosslinking results in a physically entangled, yet stable composite hydrogel. Alginate provides a fast-gelling network upon exposure to calcium ions, ensuring immediate construct formation and support. Atelocollagen, once neutralized and thermally stabilized, offers a fibrillar structure that supports cell adhesion and tissue remodeling. Rheological testing confirmed shear-thinning behavior, facilitating smooth extrusion, and compressive modulus measurements over time indicated scaffold stiffening, likely due to ECM deposition and physical entanglement between components. These findings suggest that the composite bioink maintains its structural integrity throughout printing and culture, making it suitable for regenerative applications.

The printed scaffolds demonstrated well-defined cylindrical structures with dimensions of 5 mm in diameter and 5 mm in height. The scaffolds maintained their shape post-crosslinking, confirming the effectiveness of the stabilization process. Rheological analysis indicated that the bioink exhibited shear-thinning behavior, which facilitated smooth extrusion during printing while maintaining adequate viscosity for shape retention. The structural integrity of the scaffolds was further confirmed through microscopic imaging, which showed a homogeneous distribution of cells throughout the printed constructs. Cell viability was evaluated using the LIVE/DEAD™ Viability/Cytotoxicity Kit after 5 days of culture (Figure 1B). In 2D cultures, ADMSCs exhibited a high degree of spreading, but limited 3D interactions. In contrast, 3D-printed scaffolds demonstrated enhanced cell distribution, with cells exhibiting elongated morphologies indicative of cellular interactions and integration within the scaffold matrix. Fluorescence imaging confirmed a higher proportion of live cells in the 3D environment compared to the 2D culture, emphasizing the scaffold's role in promoting cellular organization and function.

To assess the mechanical stability of the scaffolds, compressive strength was measured over 5 days of culture (Figure 1C and D). The results demonstrated a progressive increase in scaffold stiffness, suggesting enhanced structural reinforcement due to ECM deposition and cellular remodeling. The initial compressive modulus of the scaffolds was sufficient to maintain shape fidelity, while subsequent increases in stiffness indicated the formation of a more mature and resilient ECM. This mechanical adaptation over time highlights the scaffold's ability to support long-term tissue development. Animal experiments were conducted to evaluate the regenerative potential of the bioprinted constructs. A schematic overview of the experimental groups and implantation strategy was designed to assess functional integration and tissue remodeling. Preliminary observations suggest that the implanted scaffolds retained their structure and supported cellular infiltration, indicating biocompatibility and potential for *in vivo* tissue regeneration. Furthermore, to evaluate the biodegradability of the printed scaffolds, an accelerated degradation test was performed using 0.1 M NaOH at 37°C. Scaffold samples were incubated and their mass loss was measured at regular intervals over a 7-day period.[25] This study confirmed the gradual degradation of the scaffolds under alkaline conditions, which supports their potential for *in vivo* resorption. These results are presented in Figure S1, Supporting Information.

3.2. Visual and ICG video imaging

In G1, the left leg, which had undergone lymph node removal, displayed major swelling relative to the right leg (Figure 2). Upon assessment with ICG, dermal backflow was detected around the previous lymph node site, leading to a diffusion effect in the adjacent area. In G2, a comparable swelling was noted in the left leg, although it was less pronounced than that observed in G1. The level of blurring was notably less apparent in comparison to G1. In G3 and G4, no discernible differences were observed between the left and right legs. The degree of blurring observed in these groups was considerably lower than that recorded in the control group (Videos S2–S5, Supporting Information).

To quantitatively evaluate lymphedema severity and treatment response, we measured the mid-thigh circumference ratio and paw thickness ratio between the affected and contralateral hindlimbs in each experimental group (Figure 3). G1 exhibited the highest mean mid-thigh circumference ratio (1.22 ± 0.03), indicating significant edema. Similarly, G2 showed persistent swelling (1.15 ± 0.02), suggesting limited therapeutic efficacy. In contrast, G3 and G4 demonstrated significantly reduced circumference ratios (1.04 ± 0.01 and 1.02 ± 0.01, respectively; $^{***}p < 0.001$ vs. G1 and G2), indicating notable reduction in limb swelling. A similar trend was observed in paw thickness measurements. G1 and G2 exhibited elevated paw thickness ratios (1.14 ± 0.03 and 1.14 ± 0.02, respectively), whereas G3 and G4 showed significant improvement

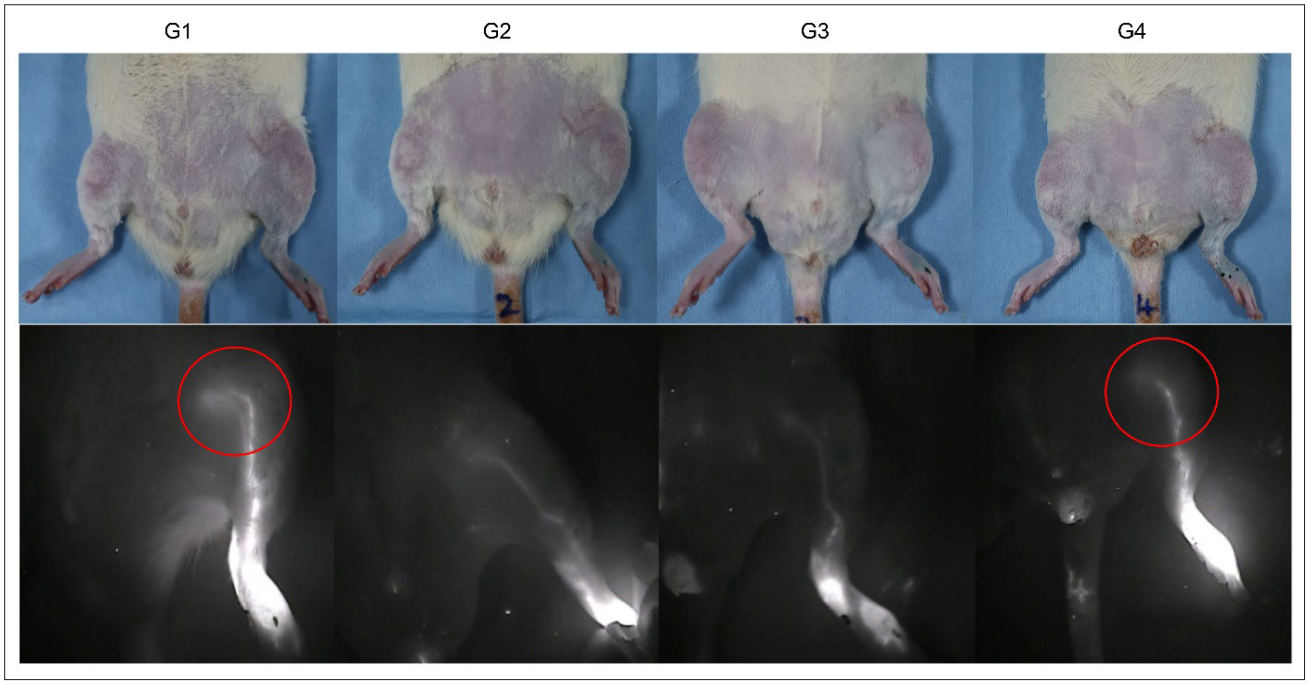

Figure 2. Visual and ICG imaging of lymphedema across experimental groups. Representative images of the hindlimbs (upper panel) and indocyanine green (ICG) video imaging results (lower panel) in each group. G1: The left leg with lymph node removal showed marked swelling and dermal backflow at the surgical site, with diffusion into surrounding areas. G2: Similar swelling was noted, but less pronounced compared to G1, with reduced dermal backflow. G3 and G4: No visible swelling or dermal backflow, and no significant differences between the left and right legs were observed.

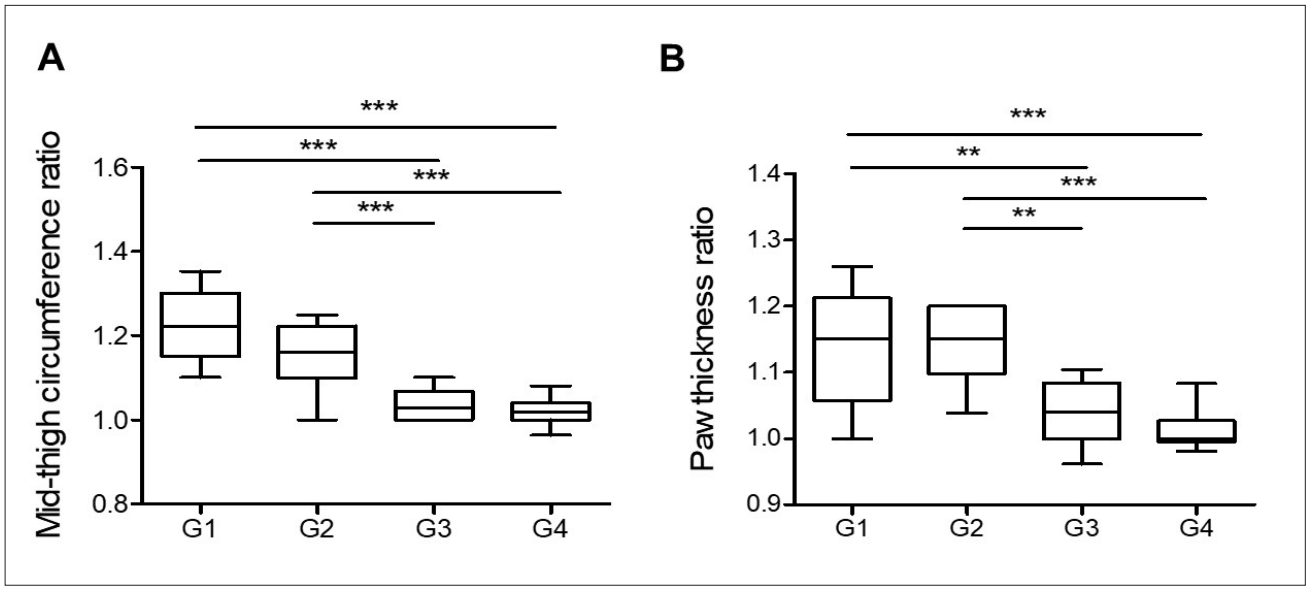

Figure 3. Boxplots comparing the mid-thigh circumference ratio (A) and paw thickness ratio (B) among the four experimental groups (G1–G4). A total of 40 rats (n = 10 per group) were evaluated. G1 and G2 exhibited significantly greater swelling than G3 and G4 in both parameters. Mean ± SEM for mid-thigh circumference ratio: G1 (1.219 ± 0.027), G2 (1.153 ± 0.024), G3 (1.035 ± 0.012), and G4 (1.018 ± 0.010). Mean ± SEM for paw thickness ratio: G1 (1.138 ± 0.025), G2 (1.141 ± 0.016), G3 (1.038 ± 0.013), and G4 (1.011 ± 0.009). Statistical analysis was performed using one-way ANOVA followed by Tukey's HSD post hoc test. Significant differences are indicated as follows: *$p < 0.05$, **$p < 0.01$, ***$p < 0.001$.

(1.04 ± 0.01 and 1.01 ± 0.01, respectively; $^{**}p < 0.01$, $^{***}p < 0.001$ vs. G1 and G2). ICG imaging revealed distinct differences in lymphatic function across experimental groups (Table 1). In G1 and G2, stage 2 dermal backflow was observed, indicating persistent lymphatic congestion. Despite clear visualization of lymphatic vessels, tracer clearance was delayed, and overall lymphatic recovery was considered poor in G1 and G2. In contrast, G3 and G4 exhibited stage 1 dermal backflow, suggesting improved lymphatic drainage. Lymphatic vessels were clearly visualized in both groups. Accordingly, both groups were assessed as having good overall recovery.

3.3. Histopathological assessment

To evaluate the effectiveness of scaffolds with hADSCs in regenerating or reconstructing lymph nodes *in vivo*, the implantation sites were examined histologically (Figure 4). In G1, glandular structures and blood vessels were distributed within the adipose tissue. No lymph node structures were observed, and small lymphocytes were sporadically scattered throughout the tissue. In G2, structures resembling normal lymph nodes were not identified. However, nodular structures were observed around blood vessels. These nodules contained a high proportion of lymphocytes, along with cells that appeared to be hADSCs, characterized by transparent microvacuolated cytoplasm and relatively large nuclei. In G3, the transplanted scaffold maintained a clearly distinguishable shape. A capsule was present along the outer border of the scaffold, although the boundary appeared indistinct in certain areas. Hematoxylin and eosin (H&E) staining revealed that small lymphocytes were predominant; however, some lymphocytes exhibited pyknosis, as indicated by their reduced nuclear size and loss of basophilic staining (Figure 4A). Masson's trichrome staining showed extensive fibrosis within the scaffold, which was attributed to the collagen-based bioprinted scaffold (Figure 4B). In G4, the scaffold containing hADSCs was transplanted, and its structure more closely resembled that of a lymph node compared to G3. A well-defined capsule was observed around the lymph node, and although overall cellularity was low, localized lymphocytic infiltration was present. H&E staining showed fewer necrotic cells compared to G3, and a higher number of cells resembling lymphocytes or hADSCs. While the proportion of viable cells was relatively high, the number of immune cells remained insufficient compared to normal lymph nodes. Masson's trichrome staining demonstrated a more clearly defined blue-stained scaffold, with numerous cells present at the scaffold interface (capsule). Among all groups, G4 exhibited the most structurally similar characteristics to a normal lymph node.

3.4. LYVE-1, Prox1, and CD31 expression by immunofluorescence

The analysis of LYVE-1, Prox1, and CD31 was conducted to assess lymphatic and vascular remodeling in lymphedema-induced tissues following 3D bioprinting scaffold implantation. LYVE-1 is a protein widely used as a marker of lymphatic vessel endothelial cells and is one of the important indicators related to lymph node formation.[26,27] Prox1 is a transcription factor essential for the differentiation and development of lymphatic endothelial cells and is one of the key markers of lymph node formation and lymphangiogenesis.[28–30]

Double staining for LYVE-1 and Prox1 revealed minimal expression in G1 and G2. In G3, LYVE-1 and Prox1 expression was observed at certain regions along the scaffold boundaries. In the scaffold containing hADSCs (G4), LYVE-1 and Prox1 expression was detected along the boundaries of the transplanted lymph node scaffold, with further increased expression within the

Table 1. Group-wise comparison of lymphatic function assessed by ICG lymphography

Group	Dermal backflow stage	Lymphatic vessel visualization	Tracer clearance	Overall lymphatic recovery
Group 1 (Control)	Stage 2	Blurred	Delayed	Poor
Group 2 (hADSC)	Stage 2	Blurred	Delayed	Poor
Group 3 (Blank scaffold)	Stage 1	Clear	Moderate	Good
Group 4 (hADSC + scaffold)	Stage 1	Clear	Rapid	Good

Notes: Dermal backflow was graded using the arm dermal backflow (ADB) scale, vessel visualization was qualitatively evaluated, and tracer clearance was classified based on fluorescence persistence.

Abbreviations: hADSCs, human adipose-derived stem cells; ICG, indocyanine green.

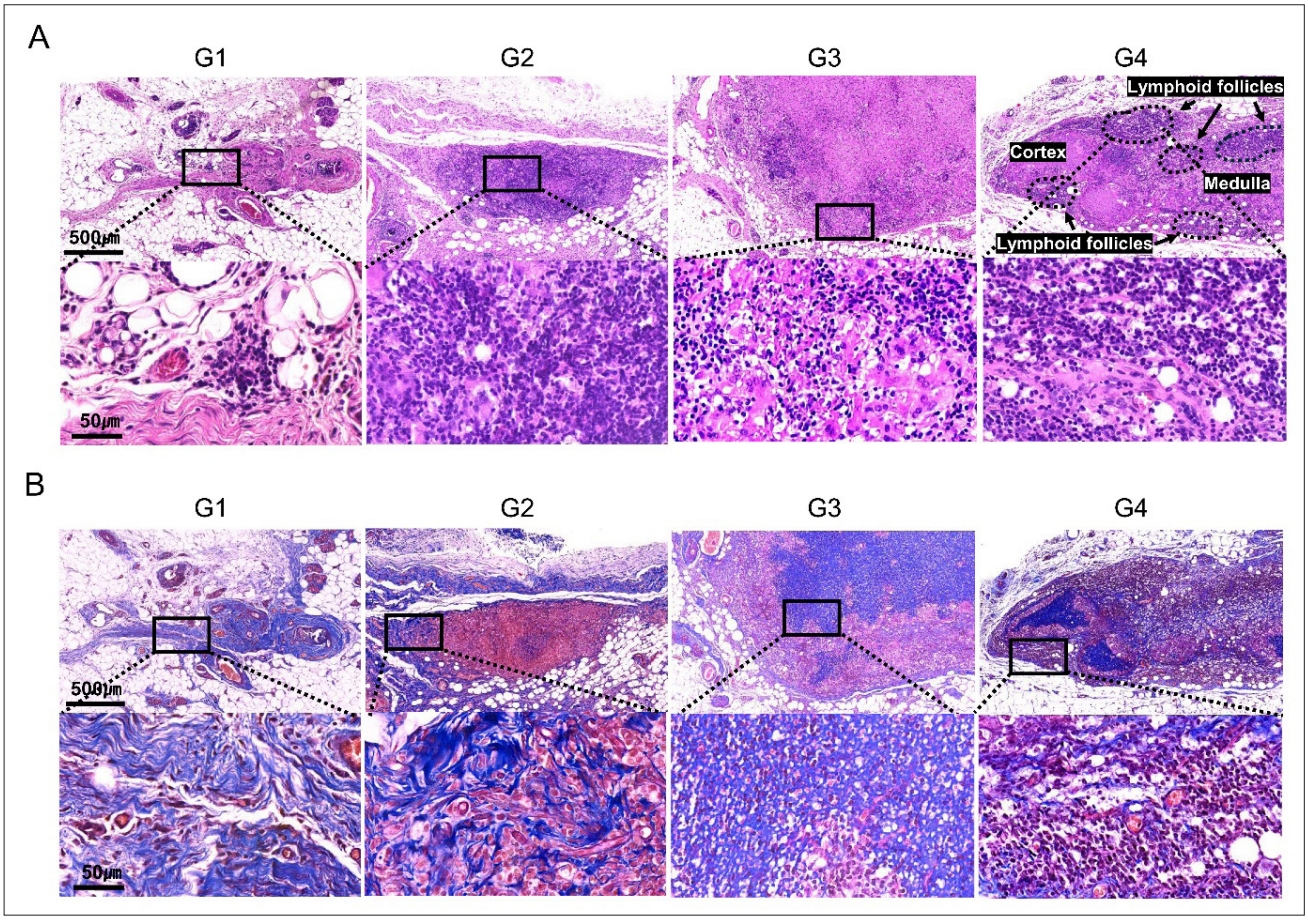

Figure 4. Histological evaluation of scaffold implants containing hADSCs for lymph node regeneration. (A) Hematoxylin and eosin staining. (B) Masson's trichrome staining. Lymphedema control group (G1): Adipose tissue with glandular structures and blood vessels, but no lymph node structures. Small lymphocytes were scattered sporadically. Human ADSCs-only (G2): Nodular structures around blood vessels containing lymphocytes and cells resembling hADSCs with microvacuolated cytoplasm and large nuclei, with no lymph node structures formed. Blank scaffold group (G3): The transplanted scaffold retained its structural integrity and was encapsulated by a fibrous capsule. Partial infiltration of immune cell clusters—including plasma cells, macrophages, and lymphocytes—was observed. Masson's trichrome staining revealed extensive fibrosis and a predominance of small lymphocytes, some exhibiting nuclear pyknosis. Human ADSC scaffold (G4): hADSC scaffold exhibited structural features most closely resembling those of native lymph nodes, including a distinct capsule, well-defined cortex and medullary-like regions, and the presence of lymphoid follicles-like structures; however, germinal center morphology was not observed. Histological analysis demonstrated widespread infiltration of plasma cells, macrophages, and lymphocytes throughout the scaffold. Compared to the blank scaffold group (G3), G4 showed fewer necrotic cells. Masson's trichrome staining revealed a well-demarcated scaffold border with dense cellularity at the periphery and localized fibrosis. Abbreviation: hADSCs, human adipose-derived stem cells.

lymph node. The expression pattern within the lymph node resembled the structure of a nodule (Figure 5). When analyzed quantitatively, LYVE-1 expression was significantly elevated in G4 (20.44 ± 2.88), compared to G3 (2.67 ± 0.25), G2 (0.80 ± 0.07), and G1 (0.34 ± 0.08) ($p < 0.001$). Similarly, Prox1 expression in G4 (20.07 ± 2.27) was significantly higher than in G3 (3.55 ± 0.15), G2 (0.61 ± 0.05), and G1 (0.47 ± 0.06) ($p < 0.001$), corresponding to a 5.7- and 42.7-fold increase over G3 and G1, respectively. When co-localization of LYVE-1 and Prox1 was quantitatively analyzed, the merged signal was markedly greater in G4 (19.07 ± 2.62), followed by G3 (3.90 ± 0.21), G2 (1.05 ± 0.02), and G1 (0.74 ± 0.03) ($p < 0.001$). The merged intensity in G4 was approximately 4.9- and 25.8-fold higher than in G3 and G1, respectively. Similarly, LYVE-1 and CD31 double staining showed increased expression in G3 and G4 compared to G1 and G2. However, distinct differences in expression patterns were observed. In G3, CD31 expression was more pronounced, with strong localization inside the scaffold rather than at its boundaries. However, no nodule-like structures were observed within the scaffold. In contrast, G4 exhibited significantly higher expression of both LYVE-1 and CD31 throughout the lymph node scaffold compared

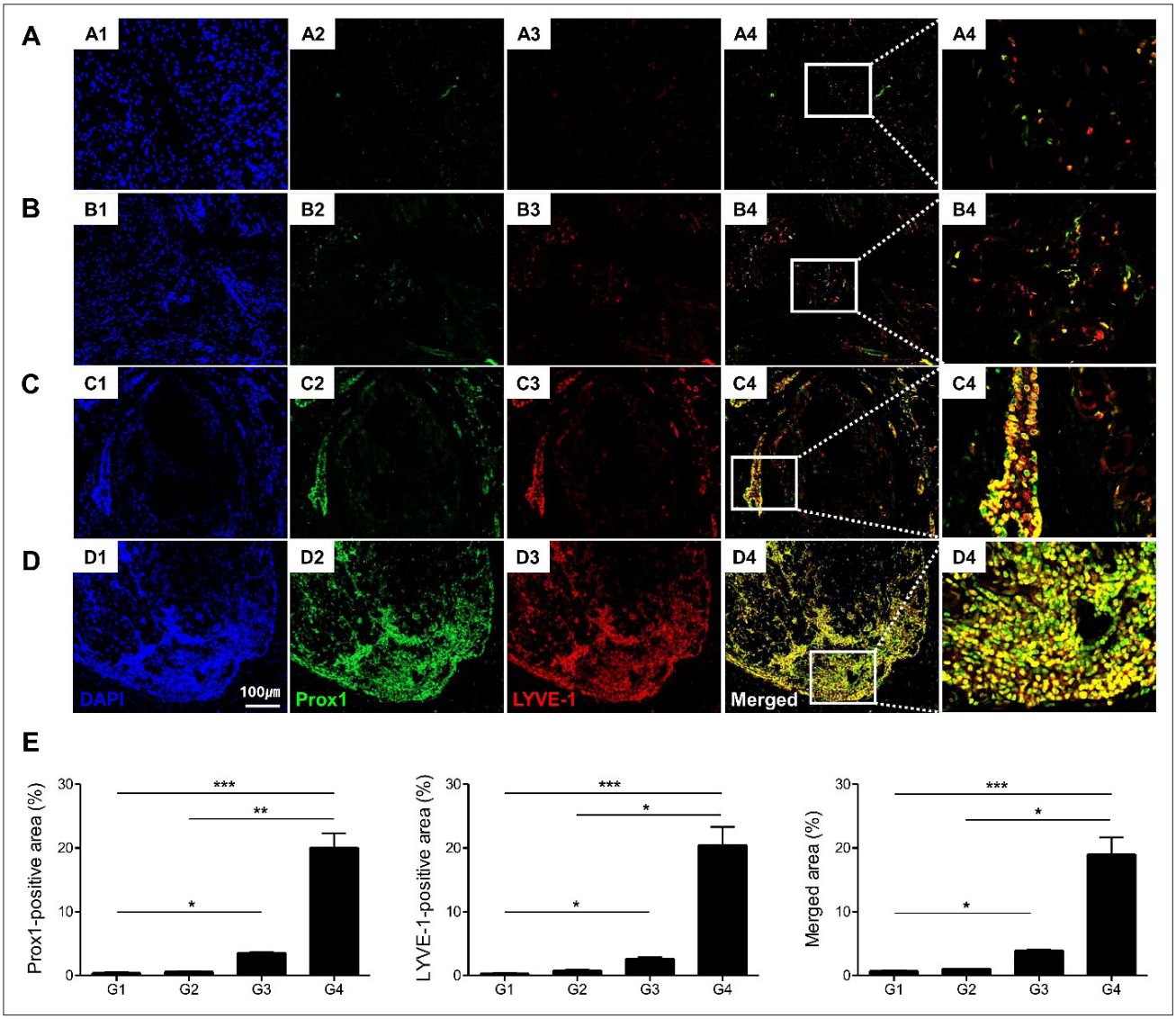

Figure 5. Double immunofluorescence staining of LYVE-1 and Prox1 to evaluate lymphatic remodeling and lymph node formation in lymphedema-induced tissues (n = 5 per group). (A) Lymphedema control group (G1), (B) hADSCs-only group (G2), (C) blank scaffold group (G3), (D) hADSCs scaffold group (G4). (A, B) Representative images show minimal expression of LYVE-1 and Prox1 in G1 and G2. (C) LYVE-1 and Prox1 expression was observed in specific areas along the scaffold boundary (lymph node capsule) with little expression in the cortex and medullary regions. (D) LYVE-1 and Prox1 expression was increased along the scaffold boundary (lymph node capsule) and overall, and was expressed in the form of lymph node cortex and medullary-like area structures. This expression pattern indicates that lymphatic vessel remodeling is promoted and lymph node-like structures are formed. Scale bar = 100 μm. (E) Quantitative analysis demonstrated significantly increased expression levels of LYVE-1 (20.44 ± 2.88), Prox1 (20.07 ± 2.27), and their merged signal (19.07 ± 2.62) in G4 compared to the other groups (***p < 0.001). Abbreviation: hADSCs, human adipose-derived stem cells.

to G3. The expression was concentrated in a thick layer around the periphery of the lymph node scaffold, distinctly separating it from the surrounding tissue. Additionally, a nodule-like structure was observed within the scaffold, suggesting the formation of a lymph node-like architecture (Figure 6). When analyzed quantitatively, CD31 was significantly upregulated in G4 (21.86 ± 2.67), compared to G3 (3.04 ± 0.42), G2 (2.20 ± 0.56), and G1 (0.95 ± 0.21) ($p < 0.001$). When co-localization of LYVE-1 and CD31 was quantitatively analyzed, the merged signal was highest in G4 (23.36 ± 3.54), followed by G3 (4.34 ± 0.45), G2 (3.33 ± 0.74), and G1 (1.79 ± 0.44) ($p < 0.001$). The merged fluorescence intensity in G4 was approximately 5.4-fold higher than in G3 and 13-fold higher than in G1. The co-localization of LYVE-1 with Prox1 or CD31 further confirms the dual remodeling of lymphatic and blood vascular networks, particularly in G4.

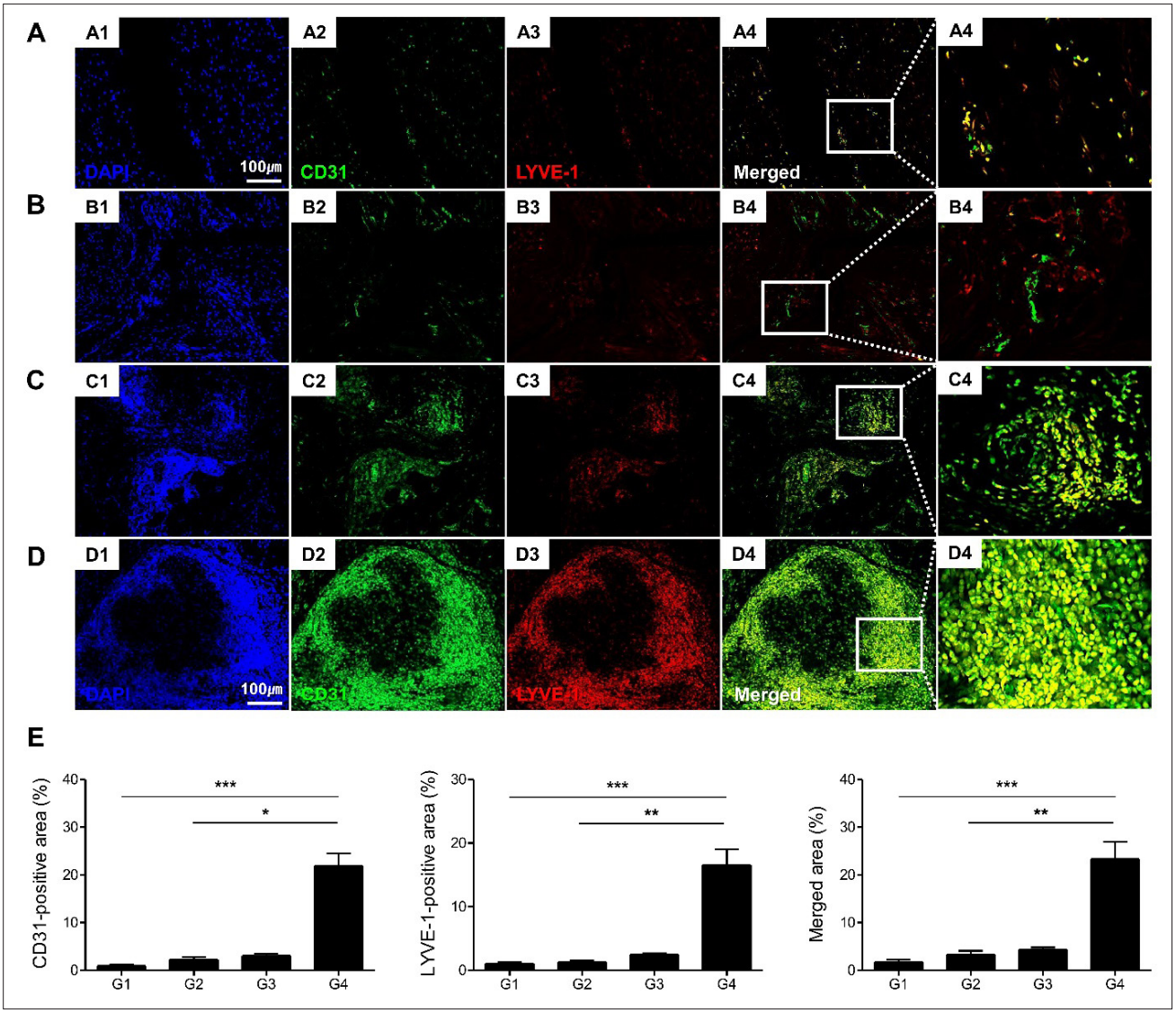

Figure 6. Double immunofluorescence staining of LYVE-1 and CD31 to assess combined lymphatic and vascular remodeling (n = 5 per group). (A) Lymphedema control group (G1), (B) hADSCs-only group (G2), (C) blank scaffold group (G3), (D) hADSCs scaffold group (G4). (A, B) Representative images show that LYVE-1 and CD31 expression is minimal in G1 and G2. (C) LYVE-1 and CD31 expression was predominantly localized within the interior of the scaffold rather than along its boundary. This distribution resembled the structural organization of lymphoid follicles, although the cortical and medullary regions could not be clearly delineated. (D) Overall, LYVE-1 and CD31 expression was clearly increased, and was more strongly expressed at the scaffold boundary (lymph node capsule). In particular, expression increased in the cortex region rather than the medullary region compared to G3. Scale bar = 100 μm. (E) Quantitative analysis results showed that the expression levels of LYVE-1 (16.54 ± 2.49), CD31 (21.86 ± 2.67), and their combined signal (23.36 ± 3.54) in G4 were significantly increased compared to the other groups (***p < 0.001). Abbreviation: hADSCs, human adipose-derived stem cells.

3.5. LYVE-1, VEGF-C, and VEGF-A protein and mRNA expression

VEGF-C is a key regulator of lymphangiogenesis, and VEGF-A, while primarily associated with angiogenesis, can also indirectly influence lymphangiogenesis through interactions with VEGFR-2 and VEGFR-3 signaling pathways.[31,32] Together, these markers provide a comprehensive understanding of the scaffold's effects on lymphatic and vascular regeneration.

The protein expression levels of LYVE-1, VEGF-C, and VEGF-A were assessed by means of Western blotting (Figure 7). The results revealed a significant increase in LYVE-1 protein expression in G4 compared to the other groups (G1, 1.00 ± 0.27-fold**; G2, 0.85 ± 0.49-fold**; G3, 0.80 ± 0.06-fold**; vs. G4, 3.34 ± 0.42-fold, $^{**}p < 0.01$, Figure 7A). Similarly, VEGF-C expression was markedly elevated in G4, with an increasing trend also observed in G2 and G3, although these changes did not reach statistical

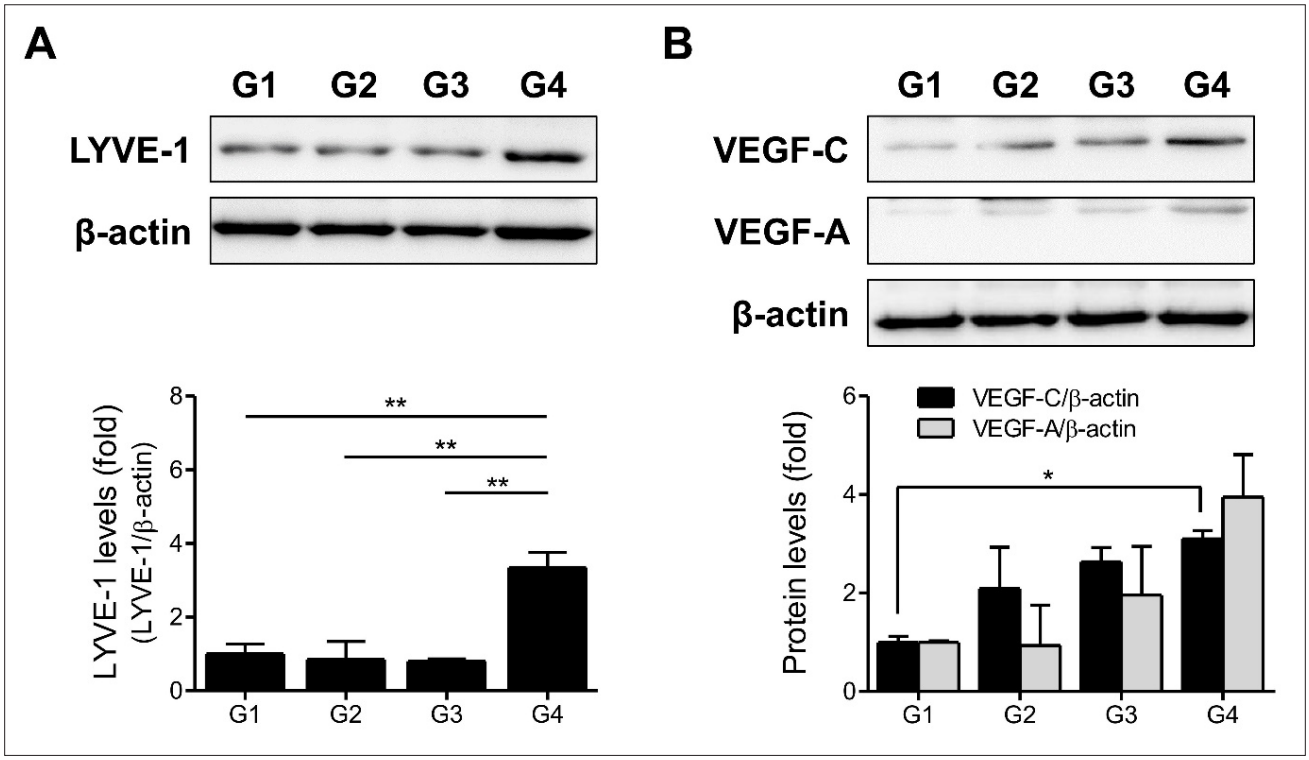

Figure 7. Protein expression of LYVE-1, VEGF-C, and VEGF-A in different treatment groups (n = 3 per group). Western blot analysis of LYVE-1 (A), VEGF-C and VEGF-A (B) protein expression in the lymphedema control (G1), hADSCs-only (G2), blank scaffold (G3), and hADSCs scaffold (G4) groups. Representative Western blot bands are shown in the upper panel, and quantification of protein expression is presented in the lower panel. Significant increases in LYVE-1 protein expression were observed in the G4 group compared to all other groups (**p < 0.01), while VEGF-C showed a gradual increase across the G2, G3, and G4 groups relative to G1; however, statistical significance was achieved only in G4 (*p < 0.05). VEGF-A protein expression showed an increasing trend in G3 and G4, although statistical significance was not achieved. Abbreviation: hADSCs, human adipose-derived stem cells.

significance (G1, 1.00 ± 0.12-fold*; G2, 2.09 ± 0.84-fold; G3, 2.64 ± 0.29-fold; vs. G4, 3.10 ± 0.17-fold, $^{*}p < 0.05$, Figure 7B). Finally, VEGF-A expression exhibited an increasing trend in G3 and G4 compared to G1, but these differences were not statistically significant (G1, 1.00 ± 0.03-fold; G2, 0.93 ± 0.82-fold; G3, 1.96 ± 0.98-fold; G4, 3.95 ± 0.86-fold, Figure 7C).

To further validate these findings, mRNA expression levels of LYVE-1, VEGF-C, and VEGF-A were analyzed using real-time PCR (Figure 8). Consistent with the protein data, LYVE-1 mRNA expression was significantly upregulated in G4 compared to all other groups, demonstrating a robust correlation between transcriptional and translational activity (G1, 1.00 ± 0.06-fold**; G2, 0.56 ± 0.16-fold**; G3, 1.27 ± 0.08-fold*; vs. G4, 2.08 ± 0.28-fold, $^{**}p < 0.01$, $^{*}p < 0.05$, Figure 8A). Similarly, VEGF-C mRNA levels were markedly increased in G4, mirroring the protein expression pattern observed in this group (G1, 1.00 ± 0.15-fold***; G2, 1.22 ± 0.04-fold***; G3, 0.92 ± 0.19-fold***; vs. G4, 2.71 ± 0.14-fold, $^{***}p < 0.001$, Figure 8B). However, unlike the protein data, VEGF-C mRNA expression in G2 and G3 did not show an increase, suggesting that the observed elevation at the protein level in these groups may involve post-transcriptional regulation. Notably, VEGF-A mRNA expression paralleled its protein expression profile, with a clear upward trend across groups and achieving statistical significance in G4 (G1, 1.00 ± 0.31-fold*; G2, 1.98 ± 0.37-fold; G3, 2.53 ± 0.17-fold; vs. G4, 3.59 ± 0.79-fold, $^{*}p < 0.05$, Figure 8C). These findings provide strong evidence that the elevated protein levels of LYVE-1, VEGF-C, and VEGF-A in the hADSCs scaffold group are primarily driven by enhanced transcriptional activity. Furthermore, these results underscore the potential role of the hADSCs scaffold group in promoting lymphangiogenesis and angiogenesis, highlighting its therapeutic potential for tissue regeneration.

4. Discussion

Surgical treatment options for lymphedema include vascularized lymph node transfer, lymphovenous anastomosis, liposuction, and excisional procedures.[33–36] Over the last 10 years, extensive research and publications

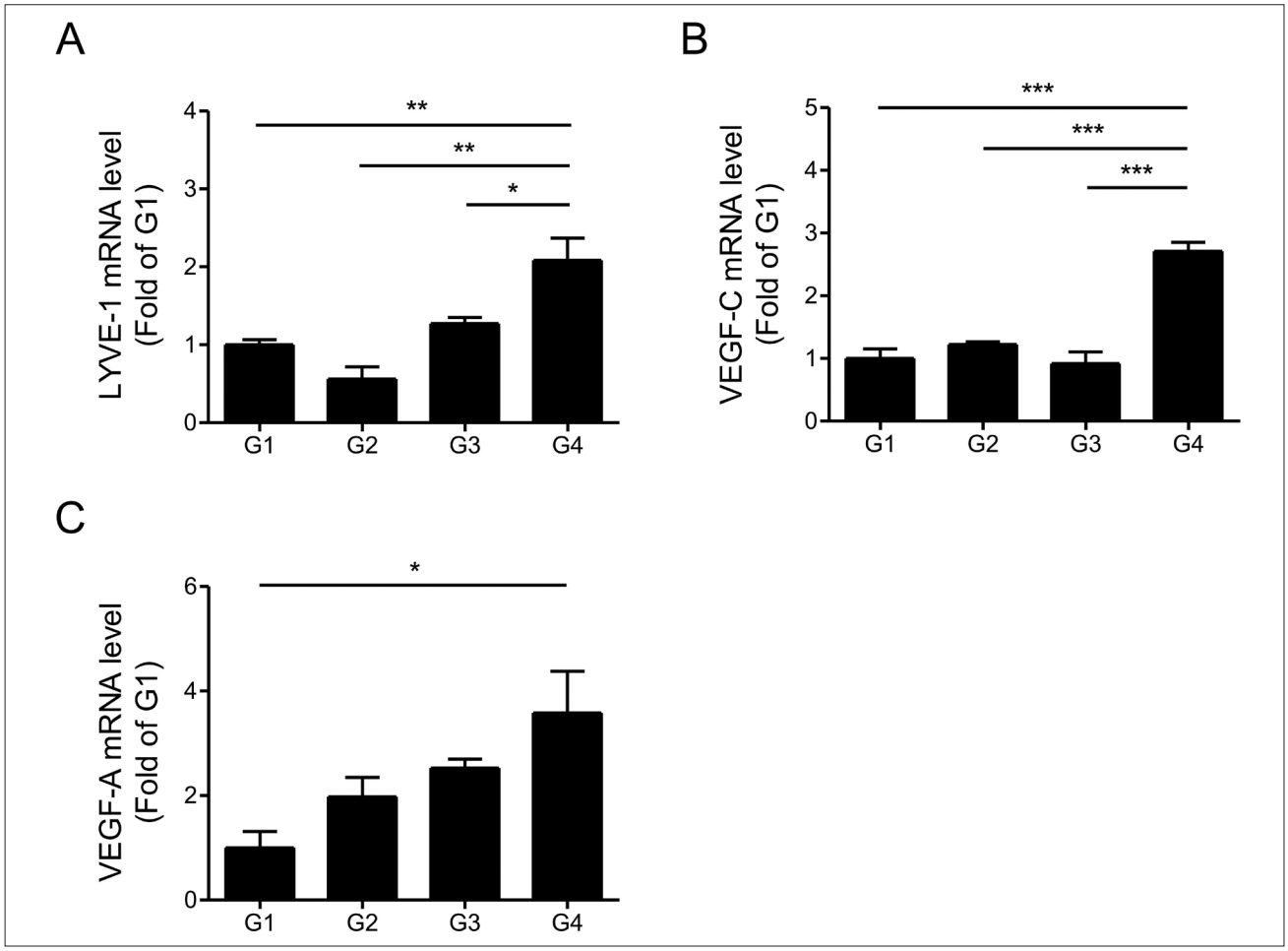

Figure 8. mRNA expression of LYVE-1, VEGF-C, and VEGF-A in different treatment groups (n = 3 per group). Real-time PCR analysis of LYVE-1 (A), VEGF-C (B), and VEGF-A (C) mRNA expression in the lymphedema control (G1), hADSCs-only (G2), blank scaffold (G3), and hADSCs scaffold (G4) groups. LYVE-1 mRNA expression was significantly elevated in G4 compared to all other groups (*$p < 0.05$; **$p < 0.01$). VEGF-C mRNA levels were also significantly increased in G4 compared to all other groups, with no significant changes observed in G2 and G3 (***$p < 0.001$). VEGF-A mRNA expression showed a significant increase in G4 compared to G1 (*$p < 0.05$). Abbreviation: hADSCs, human adipose-derived stem cells.

have focused on the surgical management of lymphedema. However, notable advancements in treatment methodologies have been limited, and each current treatment approach presents challenges. Lymphovenous anastomosis is a sophisticated procedure that necessitates advanced facilities equipped with microscopes and microsurgical instruments.[34] While some enhancement is noted shortly following the surgery, apprehensions about the progressive deterioration of lymphedema over time persist. Vascularized lymph node transfer presents a considerable risk of secondary lymphedema at the donor site where lymph nodes are extracted.[33] Consequently, there has been important research focused on techniques for regenerating lymph nodes without the necessity of harvesting them from the donor site. The researchers conducted a study indicating that the combination of hADSCs with decellularized lymph node scaffolds holds important potential for promoting lymphangiogenesis and alleviating lymphedema in animal models.[11] The authors devised an innovative technique for producing both stem cells and scaffolds through the application of 3D bioprinting technology, aimed at enhancing the efficiency of this approach. The authors contend that this development assists accurate spatial manipulation and improved functional integration of the cells with the scaffold, consequently enhancing the potential for improved therapeutic results in lymphedema treatment.

3D bioprinting is an advanced technology that employs living cells, growth factors, and biocompatible materials to construct 3D structures or tissues incrementally, layer

by layer.[37] This technology constructs scaffolds embedded with cells, creating an environment that closely resembles the architecture of native tissue, thereby assisting with cell growth, differentiation, and the development of functional tissue.[38] One of the primary advantages of 3D bioprinting is its ability to precisely control the arrangement of cells and the structure of tissues.[39] This capability can be used to enhance the replication and examination of diverse disease models.[12,40,41] Recent studies have shown the promise of 3D-printed tissues in addressing various medical issues, including bone defects, cartilage injuries, and skin wounds.[42–46] 3D bioprinting has been investigated as a means to produce personalized implants, prosthetics, and scaffolds that replicate human tissues. Also, investigations are underway regarding bioprinted vascular networks to improve the viability of transplanted tissues and organs.[47] Besides, 3D printing has shown promise in the development of customized drug delivery systems, allowing for more accurate and effective treatments for conditions such as cancer and chronic diseases.[48] As research advances, the combination of 3D printing with stem cell therapy and tissue engineering shows major potential for transforming approaches to disease treatment.[49,50]

3D bioprinting, in particular, shows great potential for addressing lymphedema by enabling the generation of regenerative lymphatic tissue, promoting lymphangiogenesis, and repairing compromised lymphatic systems.[51] 3D bioprinting can be used to fabricate scaffolds that closely resemble the architecture of lymph nodes, lymphatic vessels, or blood vessels.[51] This aids in the restoration of compromised lymphatic systems and enhances lymphatic circulation. Besides, various cell types, including hADSCs, along with biomaterials such as gelatin and collagen, are used.[52] Stem cells release growth factors essential for the formation of lymphatic vessels, and their differentiation is more efficient within a 3D structure.[53]

This research involves the implantation of 3D-bioprinted scaffolds embedded with hADSCs into lymphedema models, aimed at assisting the formation of lymphatic vessels and reinstating lymph fluid circulation. The lymphedema model was successfully validated in G1 ICG imaging, which demonstrated that the normal leg exhibited no signs of blurring, whereas the G1 showed the most important degree of blurring. The level of blurring observed in the G2, G3, and G4 was less pronounced compared to G1; however, some degree of blurring was still evident in each of these groups. This phenomenon is likely attributable to the excision of the lymph node across all groups, which may lead to a certain level of lymphatic leakage in the surrounding area, thereby reinforcing the development of the lymphedema model.

In this study, we explored how 3D-bioprinted scaffolds that include hADSCs might help encourage lymphatic and vascular remodeling in tissues affected by lymphedema. The findings showed that scaffolds with hADSCs (G4) notably boosted the expression of important markers linked to lymphangiogenesis and angiogenesis. This includes increases in LYVE-1, VEGF-C, and VEGF-A at both the protein and mRNA levels. Notably, the upregulation of these proteins is largely driven by transcriptional activity, as confirmed by real-time PCR analysis. In G4, the scaffolds displayed more noticeable structures resembling lymph nodes, along with enhanced remodeling of both lymphatic and vascular networks. This includes the development of nodule-like formations. Unlike G4, which exhibited well-organized lymph node-like structures, G3 showed only limited morphological changes without clear lymphoid architecture, and G2 did not exhibit notable therapeutic improvements in either morphological or functional assessments. This result may be attributed to the inherently low engraftment efficiency and poor retention of stem cells when delivered without a supportive matrix. Directly injected hADSCs are more susceptible to dispersion from the target site and are exposed to mechanical stress and inflammatory cytokines, which compromise cell survival and reduce their regenerative potential. These findings are consistent with our previous study, in which recellularized lymph node scaffolds incorporating hADSCs significantly enhanced lymph node regeneration and lymphatic recovery compared to simple cell injection.[11] The scaffold not only provides a structural framework for cell attachment and survival but also facilitates sustained paracrine signaling and localized therapeutic effects. Therefore, the lack of efficacy observed in G2 further supports the necessity of scaffold-mediated delivery to fully harness the regenerative capabilities of hADSCs.

In G4, we see a notable increase in VEGF-C, emphasizing its important role in the formation of lymphatic vessels. On the other hand, while VEGF-A also showed a rise in expression related to blood vessel formation, this increase did not reach statistical significance. The lymph node scaffold with hADSCs demonstrated regenerative features resembling those of a native lymph node, although it did not fully replicate the typical morphology. Histological analysis revealed distinguishable regions analogous to the cortex and medulla, along with structures reminiscent of lymphoid follicles. High-magnification observations showed cellular characteristics similar to immune cells found in normal rat lymph nodes, including the presence of plasma cells and macrophages. These findings emphasize how hADSCs-loaded scaffolds could really boost tissue regeneration, especially for restoring lymphatic function

in lymphedema. This opens up some exciting possibilities for future clinical treatments.

Although hADSCs possess multilineage differentiation potential, accumulating evidence indicates that their regenerative and immunomodulatory effects occur largely via the secretion of bioactive molecules, including VEGF, HGF, TGF-β, IGF-1, and extracellular vesicles (e.g., exosomes).[54,55] These factors promote lymphangiogenesis, modulate local immune responses, and enhance the recruitment and proliferation of host-derived progenitor cells. In our study, the use of 3D-bioprinted scaffolds embedded with hADSCs led to the formation of lymph node-like structures with notable lymphocytic infiltration, a feature not observed in the groups lacking either hADSCs or scaffold support. This suggests that the scaffold provided a protective and instructive microenvironment that stabilized hADSC viability and facilitated sustained paracrine activity. While hADSCs do not differentiate into lymphocytes, they likely contributed to the observed lymphocyte accumulation by creating a niche conducive to immune cell homing and organization.

Despite the promising findings of this study, several limitations should be acknowledged. During the 3D bioprinting process, cells may encounter stress that can adversely affect their survival rates or ability to differentiate. To tackle this issue, it is essential to advance techniques that ensure optimal conditions for cell survival throughout the printing process. The materials employed in 3D bioprinting scaffolds should be able to facilitate cell adhesion, proliferation, and differentiation. Also, scaffolds should be designed to naturally degrade over time and promote smooth integration with surrounding tissues. Beyond immediate impacts, further research is necessary to evaluate the long-term therapeutic effectiveness of 3D-bioprinted lymph tissue in the treatment of lymphedema. While structural and molecular indicators of lymphatic regeneration were evaluated, comprehensive quantitative assessments of functional lymphatic drainage were limited. Finally, the preclinical model does not fully replicate the anatomical and immunological complexity of human lymphedema, and further validation in large-animal or humanized models is necessary before clinical translation.

5. Conclusion

This study highlights the potential of 3D-bioprinted scaffolds loaded with hADSCs to promote lymphangiogenesis and improve lymphatic function in lymphedema. The scaffolds showed good cell viability, structural integrity, and enhanced lymphatic remodeling, suggesting their promising role in tissue regeneration and lymphedema treatment.

Acknowledgments

The authors would like to sincerely thank Dr. Donggu Kang, Dr. Sung-Hwan Yoon, Ms. Hayeong Cho, and Ms. Soo Young Moon for their invaluable assistance and support throughout the experiments conducted in this study.

Funding

This research was supported by a Seoul National University Bundang Hospital grant (No. 14-2019-0010) and a research fund from Honam University, 2023 (No. 2023-0151).

Conflict of interest

The authors declare they have no competing interests.

Author contributions

Conceptualization: Hyo Jin Kang, Ju-Hee Lee, Jae Hoon Jeong
Formal analysis: Hyo Jin Kang, Ju-Hee Lee
Investigation: Hyo Jin Kang, Ju-Hee Lee
Methodology: Yong Xun Jin, Yujin Myung, Jae Hoon Jeong
Writing–original draft: Hyo Jin Kang, Jae Hoon Jeong
Writing–review & editing: Ju-Hee Lee, Yujin Myung, Jae Hoon Jeong

Ethics approval and consent to participate

All experimental procedures were approved by the Institutional Animal Care and Use Committee of Seoul National University Bundang Hospital (IACUC No. BA-2308-374-002-04).

Consent for publication

Not applicable.

Availability of data

The data can be obtained by contacting the corresponding author.

References

1. Cornelissen AJM, Kool M, Keuter XHA, et al. Quality of life questionnaires in breast cancer-related lymphedema patients: review of the literature. *Lymphat Res Biol*. 2018;16(2):134-139.
doi: 10.1089/lrb.2017.0046

2. Bittar S, Simman R, Lurie F. Lymphedema: a practical approach and clinical update. *Wounds*. 2020;32(3):86-92.

3. Jørgensen MG, Toyserkani NM, Hansen FG, Bygum A, Sørensen JA. The impact of lymphedema on health-related quality of life up to 10 years after breast cancer treatment. *NPJ Breast Cancer*. 2021;7(1):70. doi: 10.1038/s41523-021-00276-y

4. Donahue PMC, MacKenzie A, Filipovic A, Koelmeyer L. Advances in the prevention and treatment of breast cancer-related lymphedema. *Breast Cancer Res Treat*. 2023;200(1):1-14. doi: 10.1007/s10549-023-06947-7

5. Thompson B, Gaitatzis K, Janse de Jonge X, Blackwell R, Koelmeyer LA. Manual lymphatic drainage treatment for lymphedema: a systematic review of the literature. *J Cancer Surviv*. 2021;15(2):244-258. doi: 10.1007/s11764-020-00928-1

6. Frese L, Dijkman PE, Hoerstrup SP. Adipose tissue-derived stem cells in regenerative medicine. *Transfus Med Hemother*. 2016;43(4):268-274. doi: 10.1159/000448180

7. Ren B, Betz OB, Seitz D, et al. Osteogenic differentiation of human adipose-derived stem cells seeded on a biomimetic spongiosa-like scaffold: bone morphogenetic Protein-2 delivery by overexpressing fascia. *Int J Mol Sci*. 2022;23(5):2712. doi: 10.3390/ijms23052712

8. Al-Ghadban S, Artiles M, Bunnell BA. Adipose stem cells in regenerative medicine: looking forward. *Front Bioeng Biotechnol*. 2022;9:837464. doi: 10.3389/fbioe.2021.837464

9. Lin HJ, Wang W, Huang YY, et al. Decellularized lymph node scaffolding as a carrier for dendritic cells to induce anti-tumor immunity. *Pharmaceutics*. 2019;11(11):553. doi: 10.3390/pharmaceutics11110553

10. Cuzzone DA, Albano NJ, Aschen SZ, Ghanta S, Mehrara BJ. Decellularized lymph nodes as scaffolds for tissue engineered lymph nodes. *Lymphat Res Biol*. 2015; 13(3):186-194. doi: 10.1089/lrb.2013.0054

11. Kang HJ, Moon SY, Kim BK, Myung Y, Lee JH, Jeong JH. Recellularized lymph node scaffolds with human adipose-derived stem cells enhance lymph node regeneration to improve lymphedema. *Sci Rep*. 2023;13(1):5397. doi: 10.1038/s41598-023-32473-z

12. Dey M, Ozbolat IT. 3D bioprinting of cells, tissues and organs. *Sci Rep*. 2020;10(1):14023. doi: 10.1038/s41598-020-70086-y

13. Gungor-Ozkerim PS, Inci I, Zhang YS, Khademhosseini A, Dokmeci MR. Bioinks for 3D bioprinting: an overview. *Biomater Sci*. 2018;6(5):915-946. doi: 10.1039/c7bm00765e

14. Arriola-Alvarez I, Jaunarena I, Izeta A, Lafuente H. Progenitor cell sources for 3D bioprinting of lymphatic vessels and potential clinical application. *Tissue Eng Part A*. 2024;30(13-14):353-366. doi: 10.1089/ten.TEA.2023.0204

15. Tripathi S, Mandal SS, Bauri S, Maiti P. 3D bioprinting and its innovative approach for biomedical applications. *MedComm (2020)*. 2022;4(1):e194. doi: 10.1002/mco2.194

16. Li X, Liu B, Pei B, et al. Inkjet bioprinting of biomaterials. *Chem Rev*. 2020;120(19):10793-10833. doi: 10.1021/acs.chemrev.0c00008

17. Levato R, Dudaryeva O, Garciamendez-Mijares CE, et al. Light-based vat-polymerization bioprinting. *Nat Rev Methods Primers*. 2023;3(1):47. doi: 10.1038/s43586-023-00231-0

18. Ng WL, Shkolnikov V. Optimizing cell deposition for inkjet-based bioprinting. *Int J Bioprint*. 2024;10(2):2135. doi: 10.36922/ijb.2135

19. Li Y, Zhang X, Zhang X, Zhang Y, Hou D. Recent progress of the vat photopolymerization technique in tissue engineering: a brief review of mechanisms, methods, materials, and applications. *Polymers (Basel)*. 2023;15(19):3940. doi: 10.3390/polym15193940

20. Malekpour A, Chen X. Printability and cell viability in extrusion-based bioprinting from experimental, computational, and machine learning views. *J Funct Biomater*. 2022;13(2):40. doi: 10.3390/jfb13020040

21. Kang D, Hong G, An S, et al. Bioprinting of multiscaled hepatic lobules within a highly vascularized construct. *Small*. 2020;16(13):e1905505. doi: 10.1002/smll.201905505

22. Yang GH, Kang D, An S, et al. Advances in the development of tubular structures using extrusion-based 3D cell-printing technology for vascular tissue regenerative applications. *Biomater Res*. 2022;26(1):73. doi: 10.1186/s40824-022-00321-2

23. Shafy SZ, Hakim M, Lynch S, Chen L, Tobias JD. Fluorescence imaging using indocyanine green dye in the pediatric population. *J Pediatr Pharmacol Ther*. 2020;25(4): 309-313. doi: 10.5863/1551-6776-25.4.309

24. Morales-Conde S, Licardie E, Alarcón I, Balla A. Indocyanine green (ICG) fluorescence guide for the use and indications in general surgery: recommendations based on the descriptive review of the literature and the analysis of experience. *Cir Esp (Engl Ed)*. 2022;100(9):534-554. doi: 10.1016/j.cireng.2022.06.023

25. Jeong CG, Hollister SJ. Mechanical, permeability, and degradation properties of 3D designed poly(1,8 octanediol-co-citrate) scaffolds for soft tissue engineering. *J Biomed Mater Res B Appl Biomater*. 2010;93(1):141-149. doi: 10.1002/jbm.b.31568

26. Jackson DG. Biology of the lymphatic marker LYVE-1 and applications in research into lymphatic trafficking and lymphangiogenesis. *APMIS*. 2004;112(7-8):526-538. doi: 10.1111/j.1600-0463.2004.apm11207-0811.x

27. Kong LL, Yang NZ, Shi LH, et al. The optimum marker for the detection of lymphatic vessels. *Mol Clin Oncol*. 2017;7(4):515-520. doi: 10.3892/mco.2017.1356

28. Shin JW, Min M, Larrieu-Lahargue F, et al. Prox1 promotes lineage-specific expression of fibroblast growth factor (FGF) receptor-3 in lymphatic endothelium: a role for FGF signaling in lymphangiogenesis. *Mol Biol Cell*. 2006; 17(2):576-584. doi: 10.1091/mbc.e05-04-0368

29. Wigle JT, Harvey N, Detmar M, et al. An essential role for Prox1 in the induction of the lymphatic endothelial cell phenotype. *EMBO J*. 2002;21(7):1505-1513. doi: 10.1093/emboj/21.7.1505

30. Harada K, Yamazaki T, Iwata C, et al. Identification of targets of Prox1 during in vitro vascular differentiation from embryonic stem cells: functional roles of HoxD8 in lymphangiogenesis. *J Cell Sci*. 2009;122(Pt 21):3923-3930. doi: 10.1242/jcs.052324

31. Onimaru M, Yonemitsu Y, Fujii T, et al. VEGF-C regulates lymphangiogenesis and capillary stability by regulation of PDGF-B. *Am J Physiol Heart Circ Physiol*. 2009;297(5):H1685-H1696. doi: 10.1152/ajpheart.00015.2009

32. Shin JW, Huggenberger R, Detmar M. Transcriptional profiling of VEGF-A and VEGF-C target genes in lymphatic endothelium reveals endothelial-specific molecule-1 as a novel mediator of lymphangiogenesis. *Blood*. 2008;112(6):2318-2326. doi: 10.1182/blood-2008-05-156331

33. Grünherz L, Barbon C, von Reibnitz D, et al. Analysis of different outcome parameters and quality of life after different techniques of free vascularized lymph node transfer. *J Vasc Surg Venous Lymphat Disord*. 2024;12(6):101934. doi: 10.1016/j.jvsv.2024.101934

34. Myung Y, Yun J, Beom J, et al. Evaluating the surgical outcome of lymphovenous anastomosis in breast cancer-related lymphedema using Tc-99m phytate lymphoscintigraphy: preliminary results. *Lymphat Res Biol*. 2024;22(2):124-130. doi: 10.1089/lrb.2023.0036

35. Lo SL, Salman M, Chen WF. Debulking lymphatic liposuction: are the therapeutic effects limited to the treated limb? *J Surg Oncol*. 2025;131(1):36-41. doi: 10.1002/jso.27985

36. Bani Monia OG, AlSaket GI, AlKadhimi AM, AlAzaideh AM, Salah BI. Multi-stage surgical debulking for advanced lower limb lymphedema: achieving cosmetic and functional success. *Cureus*. 2024;16(11):e73053. doi: 10.7759/cureus.73053

37. Pajula S, Saarikko A, Suominen S, et al. Donor-site safety in microvascular lymph node transfer for breast cancer-related lymphedema using reverse lymphatic mapping-a prospective study. *J Plast Reconstr Aesthet Surg*. 2024;98:20-31. doi: 10.1016/j.bjps.2024.08.063

38. Chen H, Zhang B, Huang J. Recent advances and applications of artificial intelligence in 3D bioprinting. *Biophys Rev (Melville)*. 2024;5(3):031301. doi: 10.1063/5.0190208

39. Lu D, Liu Y, Li W, et al. Development and application of 3D bioprinted scaffolds supporting induced pluripotent stem cells. *Biomed Res Int*. 2021;2021:4910816. doi: 10.1155/2021/4910816

40. Khanna A, Ayan B, Undieh AA, Yang YP, Huang NF. Advances in three-dimensional bioprinted stem cell-based tissue engineering for cardiovascular regeneration. *J Mol Cell Cardiol*. 2022;169:13-27. doi: 10.1016/j.yjmcc.2022.04.017

41. Sun Z, Zhao J, Leung E, et al. Three-dimensional bioprinting in cardiovascular disease: current status and future directions. *Biomolecules*. 2023;13(8):1180. doi: 10.3390/biom13081180

42. Yan Y, Li X, Gao Y, et al. Bioprinting of human neural tissues with functional connectivity. *Cell Stem Cell*. 2024;31(2):260-274.e7. doi: 10.1016/j.stem.2023.12.009

43. Sagar N, Chakravarti B, Maurya SS, Nigam A, Malakar P, Kashyap R. Unleashing innovation: 3D-printed biomaterials in bone tissue engineering for repairing femur and tibial defects in animal models - a systematic review and meta-analysis. *Front Bioeng Biotechnol*. 2024; 12:1385365. doi: 10.3389/fbioe.2024.1385365

44. Liang Q, Ma Y, Yao X, Wei W. Advanced 3D-printing bioinks for articular cartilage repair. *Int J Bioprint*. 2022; 8(3):511. doi: 10.18063/ijb.v8i3.511

45. Antezana PE, Municoy S, Álvarez-Echazú MI, et al. The 3D bioprinted scaffolds for wound healing. *Pharmaceutics*. 2022;14(2):464. doi: 10.3390/pharmaceutics14020464

46. Xie Z, Gao M, Lobo AO, Webster TJ. 3D bioprinting in tissue engineering for medical applications: the classic and the hybrid. *Polymers (Basel)*. 2020;12(8):1717. doi: 10.3390/polym12081717

47. Gupta S, Bit A. 3D bioprinting in tissue engineering and regenerative medicine. *Cell Tissue Bank*. 2022; 23(2):199-212. doi: 10.1007/s10561-021-09936-6

48. Chen EP, Toksoy Z, Davis BA, Geibel JP. 3D bioprinting of vascularized tissues for *in vitro* and *in vivo* applications. *Front Bioeng Biotechnol*. 2021;9:664188. doi: 10.3389/fbioe.2021.664188

49. Dumpa N, Butreddy A, Wang H, Komanduri N, Bandari S, Repka MA. 3D printing in personalized drug delivery: An overview of hot-melt extrusion-based fused deposition modeling. *Int J Pharm*. 2021;600:120501. doi: 10.1016/j.ijpharm.2021.120501

50. Ong CS, Yesantharao P, Huang CY, et al. 3D bioprinting using stem cells. *Pediatr Res*. 2018;83(1-2):223-231. doi: 10.1038/pr.2017.252

51. Roshangar L, Rad JS, Kheirjou R, Khosroshahi AF. Using 3D-bioprinting scaffold loaded with adipose-derived stem cells to burns wound healing. *J Tissue Eng Regen Med*. 2021;15(6):546-555. doi: 10.1002/term.3194

52. Kim M, Choi S, Choi DH, et al. An advanced 3D lymphatic system for assaying human cutaneous lymphangiogenesis in a microfluidic platform. *NPG Asia Mater*. 2024;16:7. doi: 10.1038/s41427-023-00527-3

53. Sung CJ, Gupta K, Wang J, Wong AK. Lymphatic tissue bioengineering for the treatment of postsurgical lymphedema. *Bioengineering (Basel)*. 2022;9(4):162. doi: 10.3390/bioengineering9040162

54. Chang C, Yan J, Yao Z, Zhang C, Li X, Mao HQ. Effects of mesenchymal stem cell-derived paracrine signals and their delivery strategies. *Adv Healthc Mater*. 2021; 10(7):e2001689. doi: 10.1002/adhm.202001689

55. Abdreshov SN, Demchenko GA, Yeshmukhanbet AN, et al. Morphofunctional alteration of mesenteric lymph nodes in the inflammation of the abdominal cavity. *Biology (Basel)*. 2024;13(3):166. doi: 10.3390/biology13030166